

Impact of the receiver fault distribution on aftershock activity

S. Hainzl, G. Zöller, and R. Wang (2010)

before this study,

Aftershock models are usually based either on

- purely empirical relations
- or
- deterministic calculations

However,

earthquake generation and triggering is a *complex process* consisting of a large number of unknowns

e.g.) the exact fault structure, frictional behavior, and prestress conditions



- statistical models purely based on empirical relations (e.g. ETAS model) ignore important physical knowledge and constraints, and
- deterministic simulations based only on one particular model setup are limited in their explanatory and predictive power.

in this paper,

the earthquake simulations implemented are based,

- *on the one hand,*

on realistic elastic half-space stress interactions,
rate-and-state dependent frictional earthquake nucleation,
extended ruptures with heterogeneous (frictional) slip distributions.

- *On the other hand,*

quantities like *the local orientation of fault planes*
the details of the small-scale variability
are taken from predefined probability distributions.



bridge the gap between
purely statistical and deterministic models.

Introduction [2]

■ *Stress-triggering model of aftershocks*

- Aftershocks are delayed response to ΔCFS (static Coulomb stress changes).
- $\left\{ \begin{array}{l} \text{Coseismic stress changes} \\ \text{rate-and-state frictional (RSF) response of } \textit{fault populations} \end{array} \right.$ with (Dieterich, 1994)
explain the temporal decay of aftershocks (Omori-Utsu law):

$$\lambda(t) = \frac{K}{(t + c)^p} \quad (1)$$

t : elapsed time since the main shock

$c < 1$ day

$0.8 < p < 1.2$, in most cases

these parameters depend on the main shock M
if the slip is fractal

- This stress-triggering model is in good agreement with several observation data.

Introduction [3]

■ *Spatial distribution of aftershocks*

- In contrast to the temporal decay,
the spatial aftershock patterns are less understood.

- Recent studies suggested that
the aftershock activity decays with a *power law*: $\sim d^{-\eta}$.

(d : distance from the main shock rupture)

Felzer and Brodsky (2006): $\eta \approx 1.3 - 1.5$, from the near to the far field

- ▶ Richards-Dinger and Stein (2009) questioned because the considered background activity is inappropriate.

Such a small η indicate *dynamic stress triggering*.

Introduction [3]

■ *Spatial distribution of aftershocks*

- Furthermore, regions of *reduced activity*, as predicted by the static stress triggering model in the stress shadows ($\Delta\text{CFS} < 0$), *have been identified only in a few cases.*

Some recent studies demonstrate that the small-scale slip (not be accessible to direct measurements) could explain the absence of quiescence.

- For the 1992 Landers aftershock sequence, the static stress-triggering model fits the observation well, if uncertainties of stress computations are taken into account (Hainzl et al., 2009).

$\eta = 1.3$, within the first 50 km.



- It is still an open scientific issue whether static or dynamic or both types of stress changes are the driving force of aftershocks.

Introduction [4]

■ *Uncertainties in the stress calculation*

- The stress-triggering model rely on *the reliable determination of stress changes*.

- However,
the stress calculations consists of *large uncertainties*:

[i] The inversion results for *the slip model are nonunique*.
Spatial inhomogeneities of material and prestress are ignored.

[ii] The effect of aftershock interactions (secondary stress changes)
is ignored, in most investigations.

[iii] Aftershock are typically calculated only for two ideal cases:
(1) *a fixed receiver fault mechanism*
(2) *optimally oriented fault planes*

▶ However, real earthquakes will be able to nucleate
with some probability on all faults existing.

- In this paper,
the impact of earthquake nucleation *on distributions of receiver fault orientations*
for the spatiotemporal aftershock patterns is investigated.

Model [5]

■ *Steps of the model simulation*

- The model simulation consists of following three steps:
 - 1: a main shock slip distribution is calculated;
 - 2: the induced Coulomb stress changes are calculated *for different earthquake mechanism*;
 - 3: the resulting earthquake activity is calculated assuming RSF properties.

Model: Main shock [6]

■ Calculation of main shock

- The size of the rupture area A is calculated (Wells and Coppersmith, 1994):

$$A = 10^{-3.49+0.91M} (\text{km}^2) \quad M: \text{ given main shock magnitude}$$

- Square ruptures are assumed, if the down-dip end fits into the seismogenic depth. Otherwise, the length of the rupture is extended:

$$L = A \cdot \sin(\text{dip}) / z_{MAX}$$

- The mean slip on this rupture area is calculated by the magnitude-moment relation of Kanamori and Anderson (1975).

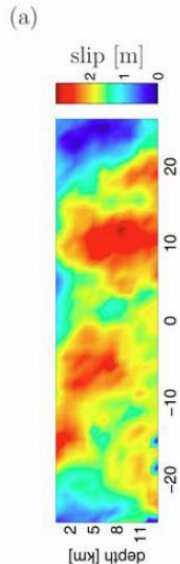


(Fig. 1a)

Model: Main shock [7]

■ *Heterogeneous slip on fault*

- *Very heterogeneous slip patterns on faults* are often shown in slip inversions.
- Scale-invariant slip models (fractal slip models) have been proposed:

For a two-dimensional fractal model,

$$u(k) \propto k^{-1-H} g(k)$$

$u(k)$: slip

$g(k)$: a realization of a Gaussian white noise

k : the wave number

H : the Hurst exponent related to the fractal dimension $D = 3 - H$

- $H = 0.71 \pm 0.23$, from the analysis of the slip distributions of 44 earthquakes (Mai and Beroza, 2002).
- In this simulation, random slip distributions with patch dimension of 1 km and a Hurst exponent of 0.7 are used.

Model: Static Coulomb Stress Changes [8]

■ Coulomb stress changes

- Coulomb stress changes are defined according to

$$\Delta\text{CFS} = \Delta\tau + \mu(\Delta\sigma + \Delta p) \quad (2)$$

$\Delta\tau$: the shear stress changes calculated along the slip direction (rake angle) on the assumed fault plane

$\Delta\sigma$: the normal stress changes (positive for extension)

μ : the friction coefficient

Δp : the pore pressure changes

- According to constant apparent friction model,

$$\Delta p = -B\Delta\sigma$$

B : Skempton coefficient ($0 \leq B \leq 1$)

- Thus, (2) can be written as

$$\Delta\text{CFS} = \Delta\tau + \mu_{\text{eff}}\Delta\sigma$$

with the effective coefficient $\mu_{\text{eff}} = (1 - B)\mu$

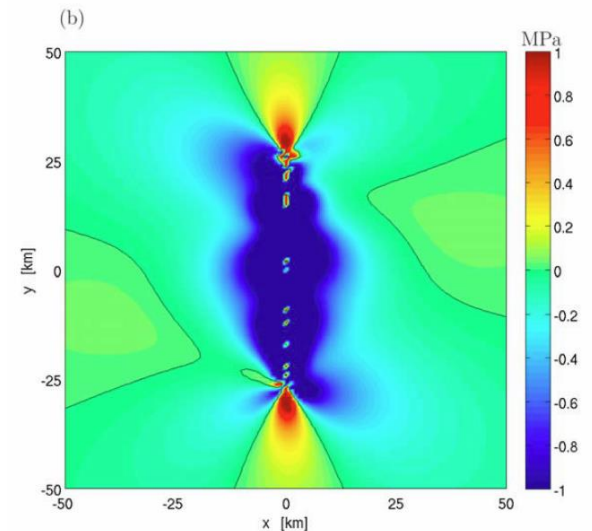


(Fig. 1b)

Model: Receiver Fault Distribution [9]

■ *Two approaches for the calculation of Coulomb stress changes*

- *The knowledge of the geometry and the faulting mechanism of the target faults is required for the calculation of Coulomb stress changes.*
- Two approaches are commonly adopted:
 - (1) Prescribed faulting mechanism
(i.e., to assign strike, dip, and rake angles of the target faults based e.g., on geological constraints)
 - (2) Calculated optimally oriented planes for Coulomb failure

In this case,
the magnitude and the orientation of the principal axes
of the regional stress field σ^r has to be known.

Then, earthquakes will occur on that fault plane orientation
which maximizes the Coulomb stress for the total stress tensor
defined as $\sigma^{tot} = \sigma^r + \Delta\sigma$
where $\Delta\sigma$ is the coseismic stress perturbation.

Model: Receiver Fault Distribution [10]

■ *Unrealistic settings of preexisting faults*

- In both cases, earthquake nucleation is only considered to occur on *one particular fault orientation*.
- Both cases are rather *unrealistic* because...
 - (1) large uncertainties are involved in the calculation of the relevant fault plane,
 - (2) the seismogenic crust is typically fractured in a complex way and thus potential receiver faults will have, in general, *a distribution of orientations* where earthquakes are able to nucleate.

Model: Receiver Fault Distribution [11, 12]

■ *Distributions of receiver fault orientation*

- In this model, the orientation of receiver faults is described *by a distribution function*.
- It is assumed for simplicity that the distribution of receiver fault orientation is everywhere the same and that it is separable with respect to the strike and dip angles:

$$f(\text{strike}, \text{dip}) = f_1(\text{strike}) \cdot f_2(\text{dip}) \cdot \sin(\text{dip})$$

(the dip orientations follow a $\sin(\text{dip})$ -distribution)

- The strike and dip distributions f_1 and f_2 are assumed for three cases:
 - (1) *fixed values*, i.e., Dirac delta density functions;
 - (2) *Gaussian distributions*;
 - (3) *a uniform distribution*. } end-member models (1), (3) and an intermediate case (2)
- In practice, the corresponding relative frequency is calculated and weighted for each possible combinations (indexed with i):

$$w_i = \frac{f_1(\text{strike}_i) \cdot f_2(\text{dip}_i)}{\sum_{k,l} f_1(\text{strike}_k) f_2(\text{dip}_l)}$$

Model: Rate-and-State Frictional Rupture Nucleation Model [13]

■ *The framework of RSF*

- The framework of rate-and-state friction (Dieterich, 1994; Dieterich et al., 2000) is used to relate stress changes to earthquake.
- In this theory, the seismicity rate R is inversely proportional to the state variable γ :

$$R(t) = \frac{r}{\dot{\tau}\gamma(t)} \quad (3)$$

r : the stationary background rate

$\dot{\tau}$: the tectonic loading rate

The evolution of the state variable as a function t and τ is given by

$$d\gamma = \frac{dt - \gamma d\tau}{A\sigma} \quad (4)$$

A : a dimensionless fault constitutive parameter usually ~ 0.01

Model: Rate-and-State Frictional Rupture Nucleation Model [13]

■ *The framework of RSF*

- Normal stress changes can be taken into account by an additional parameter α (for $\Delta\sigma \ll \sigma$)

- Then the same evolution law,

$$d\gamma = \frac{dt - \gamma d\text{CFS}}{A\sigma}$$

holds for the equivalent Coulomb stress $\text{CFS} = \tau + (\mu - \alpha)(\sigma + p)$
(α is usually set to 0.25)

- According to the constant apparent friction model (section 2.2), CFS is the Coulomb stress calculated with $\mu_{\text{eff}} = (\mu - \alpha)(1 - B)$.

$$\Delta\text{CFS} = \Delta\tau + \mu_{\text{eff}}\Delta\sigma$$

- In the calculation of this study,

$$\mu = 0.75, B = 0.5, \text{ and } \alpha = 0.25, \text{ leading to } \mu_{\text{eff}} = 0.25$$

Model: Rate-and-State Frictional Rupture Nucleation Model [14, 15]

■ Time-dependent earthquake rate and the total number of events

- For a single stress jump ΔCFS ,
(4) yields the time-dependent earthquake rate

$$R(t) = \frac{r}{1 + \left(e^{-\frac{\Delta CFS}{A\sigma}} - 1 \right) e^{-\frac{\Delta t}{t_a}}} \quad (5)$$

Δt : the elapsed time after the stress step
 t_a : the aftershock relaxation time $\equiv A\sigma/\dot{\tau}$

- In the case of a sequence of stress jumps,
the evolution law (4) can be solved by iteration (Haizl, 2009).
- The total number of earthquakes in the time period T is

$$\begin{aligned} N(T) &= \int_0^T R(t) dt \\ &= \frac{r}{\dot{\tau}} \left[A\sigma \log \left(e^{-\frac{\Delta CFS}{A\sigma}} + e^{\frac{T}{t_a}} \right) + \Delta CFS \right] \end{aligned} \quad (6)$$

Model: Model Parameters [16]

■ Background rate and frictional resistance

- The earthquake activity depends mainly on two parameters:

- (1) background rate r
- (2) frictional resistance $A\sigma$

$$R(t) = \frac{r}{1 + \left(e^{-\frac{\Delta CFS}{A\sigma}} - 1 \right) e^{-\frac{\Delta t}{t_a}}}$$

- the tectonic loading rate $\dot{\tau}$, or the aftershock relaxation time $t_a \equiv A\sigma / \dot{\tau}$ is an additional parameter, in principle.

However,

$\dot{\tau}$ is correlated with r

because the seismic moment released by the background activity has to equal the seismic moment induced by tectonic loading (Catalli et al., 2008):

$$\dot{\tau} = \langle \Delta\tau \rangle \cdot r \quad (7)$$

$$\langle \Delta\tau \rangle \equiv \frac{10^{9.1+1.5M_{\min}}}{SW_{\text{seis}}} \frac{b}{1.5 - b} \left(10^{(1.5-b)(M_{\max}-M_{\min})} - 1 \right) \quad (8)$$

S : the area

W_{seis} : the thickness of the seismogenic volume ($= z_{\max} - z_{\min}$)

Model: Model Parameters [17]

■ Independent parameters of the rate-and-state model



$$\dot{\tau} = \langle \Delta\tau \rangle \cdot r$$
$$\langle \Delta\tau \rangle \equiv \frac{10^{9.1+1.5M_{\min}}}{SW_{\text{seis}}} \frac{b}{1.5-b} (10^{(1.5-b)(M_{\max}-M_{\min})} - 1)$$

- Thus, knowing

{ the background seismicity rate (r) ,
the frequency-size distribution (b, M_{\max}, M_{\min}) ,
the seismogenic thickness (W_{seis}) ,

the tectonic loading $(\dot{\tau})$ is fixed and

the rate-and-state model consists *only two independent parameters*, r and $A\sigma$

- Furthermore,

taking the relation $\dot{\tau} = \langle \Delta\tau \rangle \cdot r$ (7) into (6) yields that

$$N(T) = \frac{1}{\langle \Delta\tau \rangle} \left[A\sigma \log \left(e^{-\frac{\Delta CFS}{A\sigma}} + e^{\frac{\langle \Delta\tau \rangle r T}{A\sigma}} - 1 \right) + \Delta CFS \right] \quad (\because t_a = \frac{A\sigma}{\langle \Delta\tau \rangle \cdot r})$$

which is *only weakly dependent on the background rate r*

Model: Model Parameters [18]

■ Earthquake rate for multiple receiver fault orientation

- The earthquake rate on faults with a certain orientation (index i) is proportional to the loading rate $\dot{\tau}$
- The earthquake rate is

$$r_i = \frac{r w_i \dot{\tau}_i}{\sum_i w_i \dot{\tau}_i} = \frac{r w_i g_i}{\sum_i w_i g_i}$$

w_i : the relative number of faults with orientation i (see section 2.3)

g_i : the fraction of shear loading on plane i relative to the shear stress loading on the plane optimally oriented to the tectonic stressing $\dot{\tau}_0$ ($=\frac{\dot{\tau}_i}{\dot{\tau}_0}$)

(the slip direction (rake vector) is in the direction of maximum loading.)

- $\dot{\tau}_0$ is given by the condition that

$$\dot{\tau}_0 = \sum_i g_i r_i \langle \Delta \tau \rangle = r \langle \Delta \tau \rangle \frac{\sum_i w_i g_i^2}{\sum_i w_i g_i}$$

where the unloading due to earthquake on the different planes must compensate the tectonic loading.

Simulations [19]

■ *Settings*

- The aftershock activity following hypothetical M7.0 right-lateral strike slip main shocks is considered.
- Analyzed aftershock rate $R(x, y, z, t)$ is in 200×200 km box and depth interval from 5 to 15 km.
- *A spatially uniform background rate r (N events per year) according to Gutenberg-Richter frequency-magnitude distribution ($\log[N(> M)] = a - bM$) with $b = 1$ is assumed.*
The simulation is performed with *a values of 3, 4, and 5 per 10^4 km²*
- *Three difference values of $A\sigma$ ($=0.01, 0.05, 0.1$ Mpa) are used based on the previous observations.*

Simulations [20-26]

■ *The simulation steps*

- For a given uniform background rate r and friction parameter $A\sigma$, the simulation steps are then the following:
 1. Choosing *the receiver fault orientations*:
 - (i) only one orientation (fixed)
 - (ii) all possible orientations (uniform)
 - (iii) Gaussian-distributed strike- and dip- orientations (Gaussian)
 2. Calculation of the *aftershock duration time* $t_{a,i}$ and *the background rate* r_i for each receiver fault orientation

Simulations [20-26]

■ The simulation steps

3. Creating a main shock slip distribution ▶

4. Calculation of the Coulomb stress changes ▶
with the analytic formulas (Okada, 1992)
at each grid node

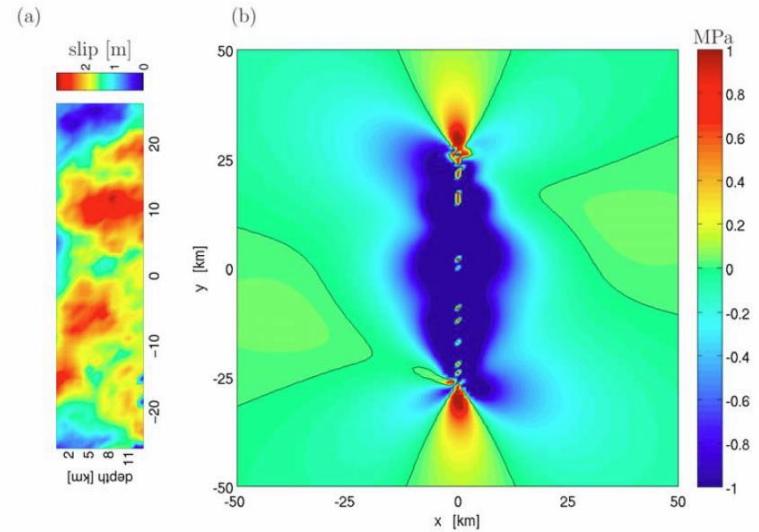


Figure 1. (a) Example of a main shock slip model with the Hurst exponent of 0.7 used in our analysis. (b) Corresponding stress changes on receiver faults with the same mechanism as the main shock at 10 km depth. The black line defines the locations with zero stress change.

5. Determination of the total earthquake rate R (eq. 5)
at each location by summing over the activity on
the different receiver fault planes:

$$R(x_k, y_k, z_k, t) = \sum_i R(\Delta CFS_i, r_i, A\sigma, ta_i, t)$$

Simulations [20-26]

■ *The simulation steps*

6. Analysis of the resulting activity:

(i) the temporal decay of the total activity

$$R(t) = \sum_k R(x_k, y_k, z_k, t)$$

(ii) the activity map

$$R(x, y) = \sum_k \int_{t_0}^T R(x, y, z_k, t) dt$$

(iii) the distance-dependent activity $R(d)$

(d is the nearest distance to the main shock rupture)

- The time integration is performed from $t_0 = 1$ (s) to $T = 1$ (year).

Results, Spatiotemporal Pattern [27, 28]

■ Temporal aftershock decay

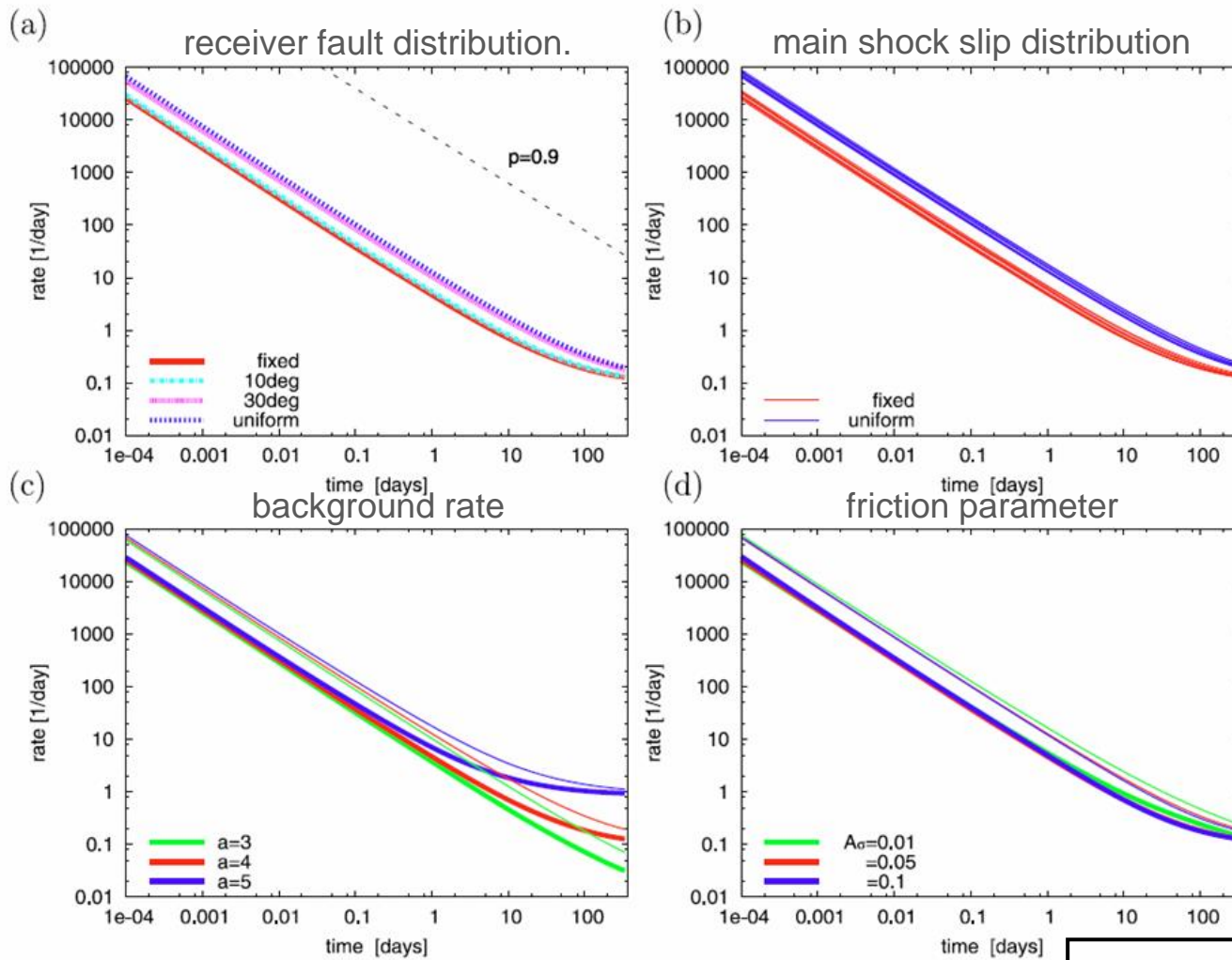


Figure 2

$$R(t) = \sum_k R(x_k, y_k, z_k, t)$$

Results, Spatiotemporal Pattern [27]

■ *Temporal aftershock decay: different receiver fault distribution*

- For all different receiver distribution, the decay follows a power law (Omori law, with $p \approx 0.9$)
- However, the aftershock productivity is significantly enhanced if broader distribution of receiver fault orientations are considered.

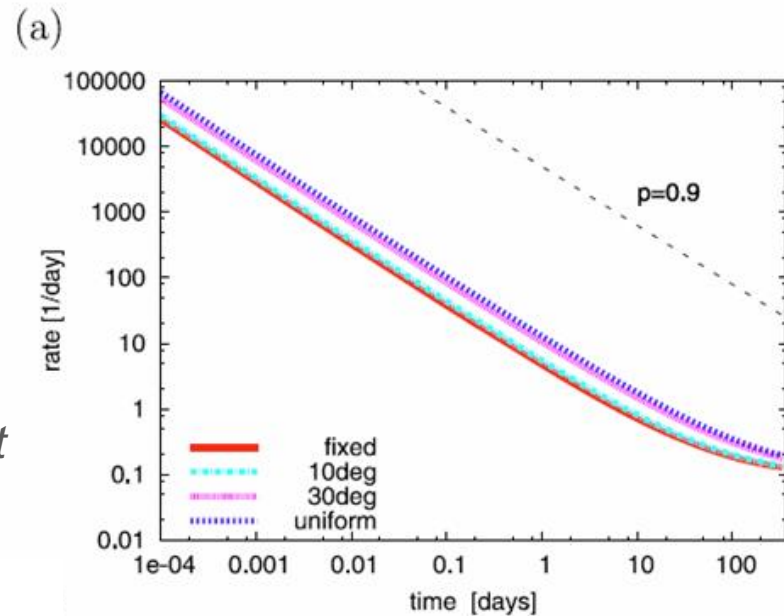


Figure 2a

Results, Spatiotemporal Pattern [27]

■ *Temporal aftershock decay: different main shock slip distributions*

- The resulting variability is much smaller than the changes resulting from the different receiver fault distributions.

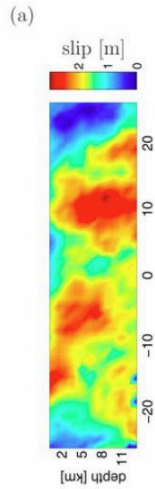


Figure 1a

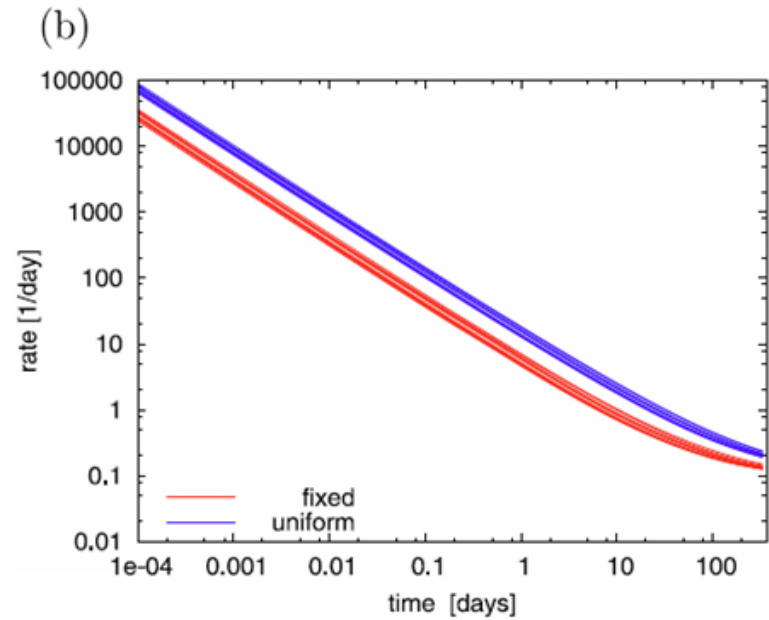


Figure 2b

Results, Spatiotemporal Pattern [28]

■ Temporal aftershock decay: different RSF parameters

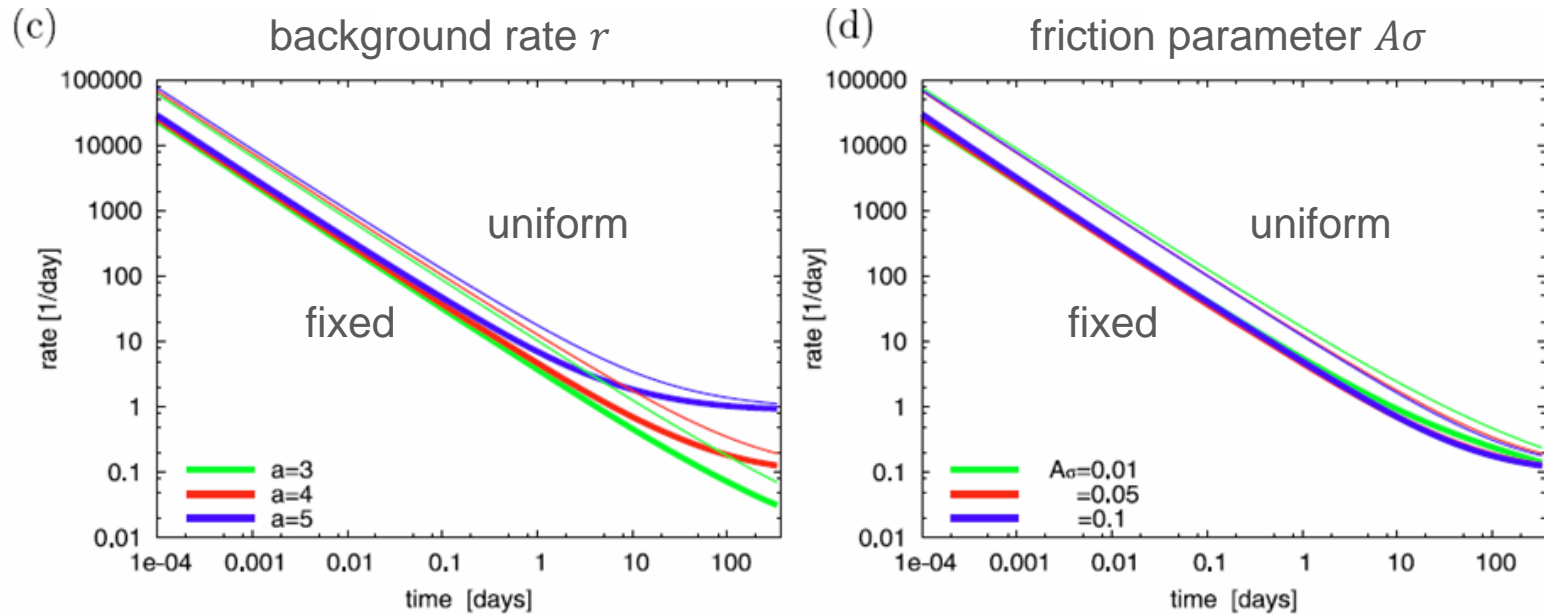


Figure 2c, d

- The other values of the background rate r and friction parameter $A\sigma$ produced almost the same result.
- It seems to contradict the equation (5), but, as a result of the linear relation between r and $\dot{\tau}$, the total activity becomes almost independent of the seismicity level (section 2.4)

Results, Spatiotemporal Pattern [29-31]

■ Spatial aftershock decay

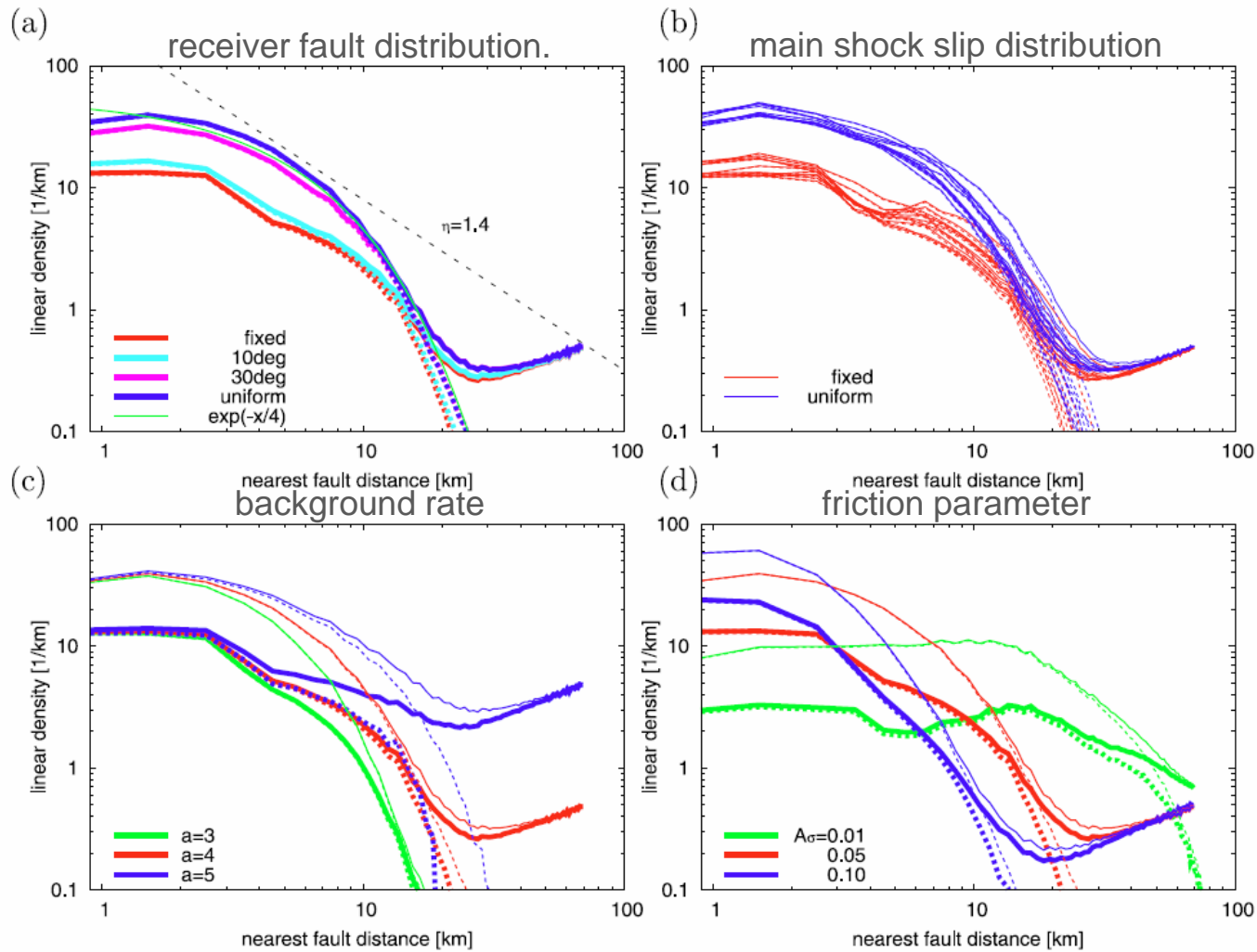


Figure 3

Results, Spatiotemporal Pattern [29]

■ *Spatial aftershock decay: different receiver fault distribution*

- Broader distributions of receiver fault orientations leads to a smoother decay.
- If a uniform distribution of receiver faults exist, the spatial decay is close to *an exponential function*
- For fixed receivers, it is more *power-law-like* with $\eta \approx 1.4$

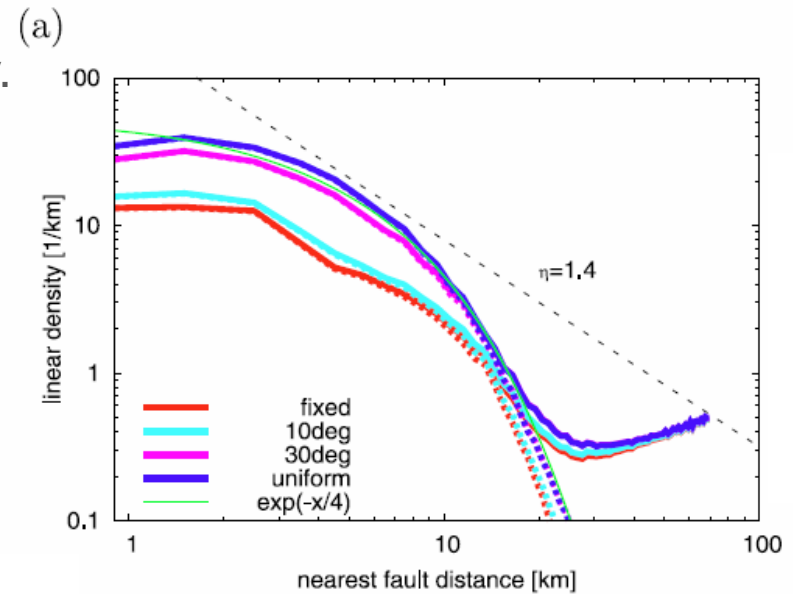


Figure 3a

Results, Spatiotemporal Pattern [30]

■ *Spatial aftershock decay: different main shock slip distributions*

- The details of the main shock slip distribution have a bigger effect on the density-distance distribution than on the temporal decay.
- However, this variability is again smaller than the that from the receiver distribution.

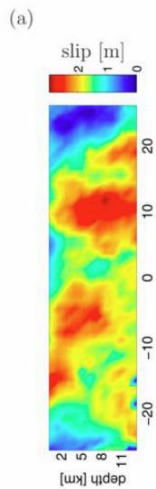


Figure 1a

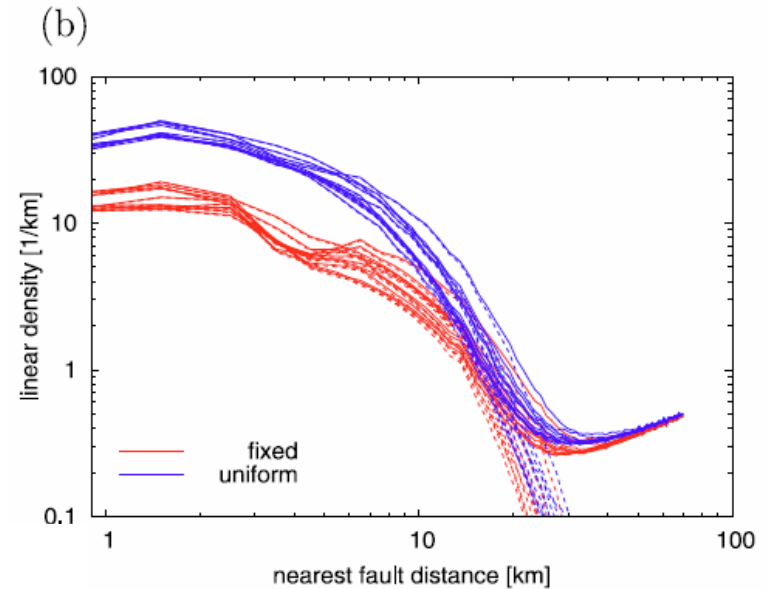


Figure 3b

Results, Spatiotemporal Pattern [30]

■ *Spatial aftershock decay: different background rate*

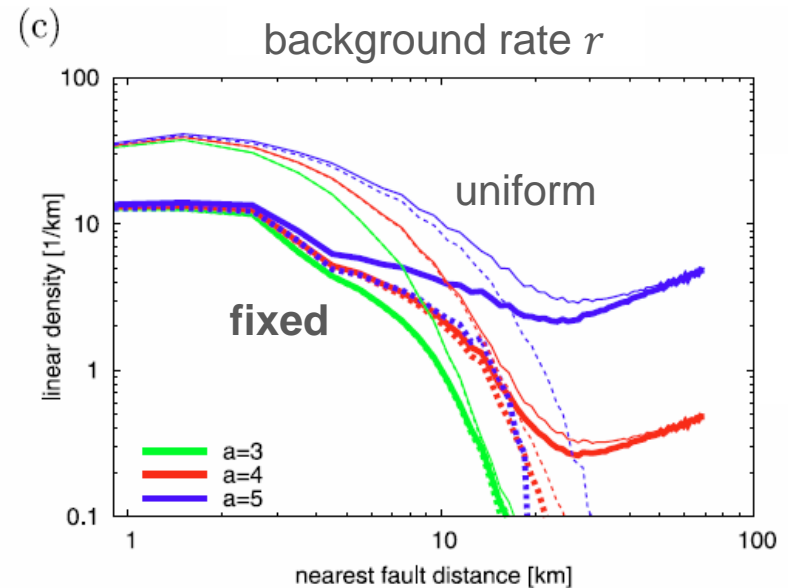


Figure 3c

- Different levels of the background seismicity do not change the activity close to the main shock rupture, but affect significantly the shape of the decay at larger distance, mainly due to the convergence of the earthquake activity to the background level.

Results, Spatiotemporal Pattern [31]

■ Spatial aftershock decay: different friction parameter

- The frictional parameter $A\sigma$ has a similar *strong impact* as the receiver fault distribution.
- The distribution becomes broader and the maximum density decreases for smaller $A\sigma$ values.

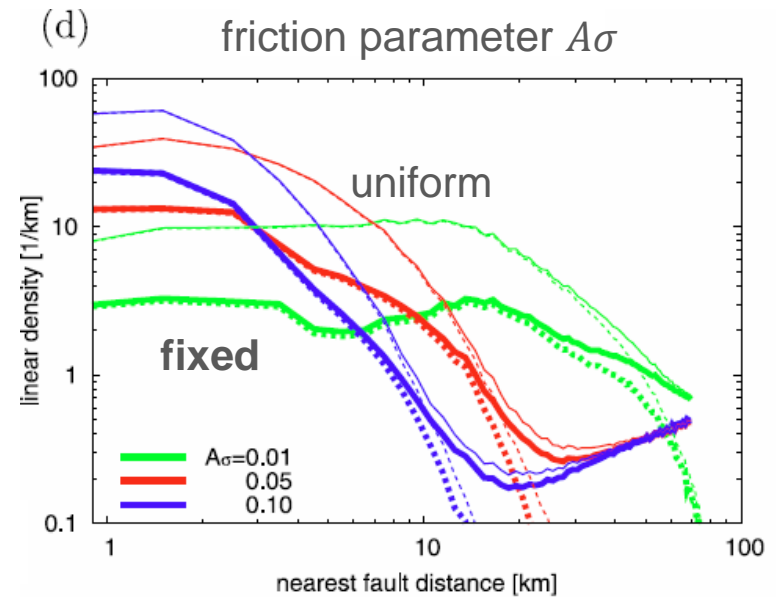


Figure 3d

Results, Spatiotemporal Pattern [32, 33]

■ *Spatial activation map*

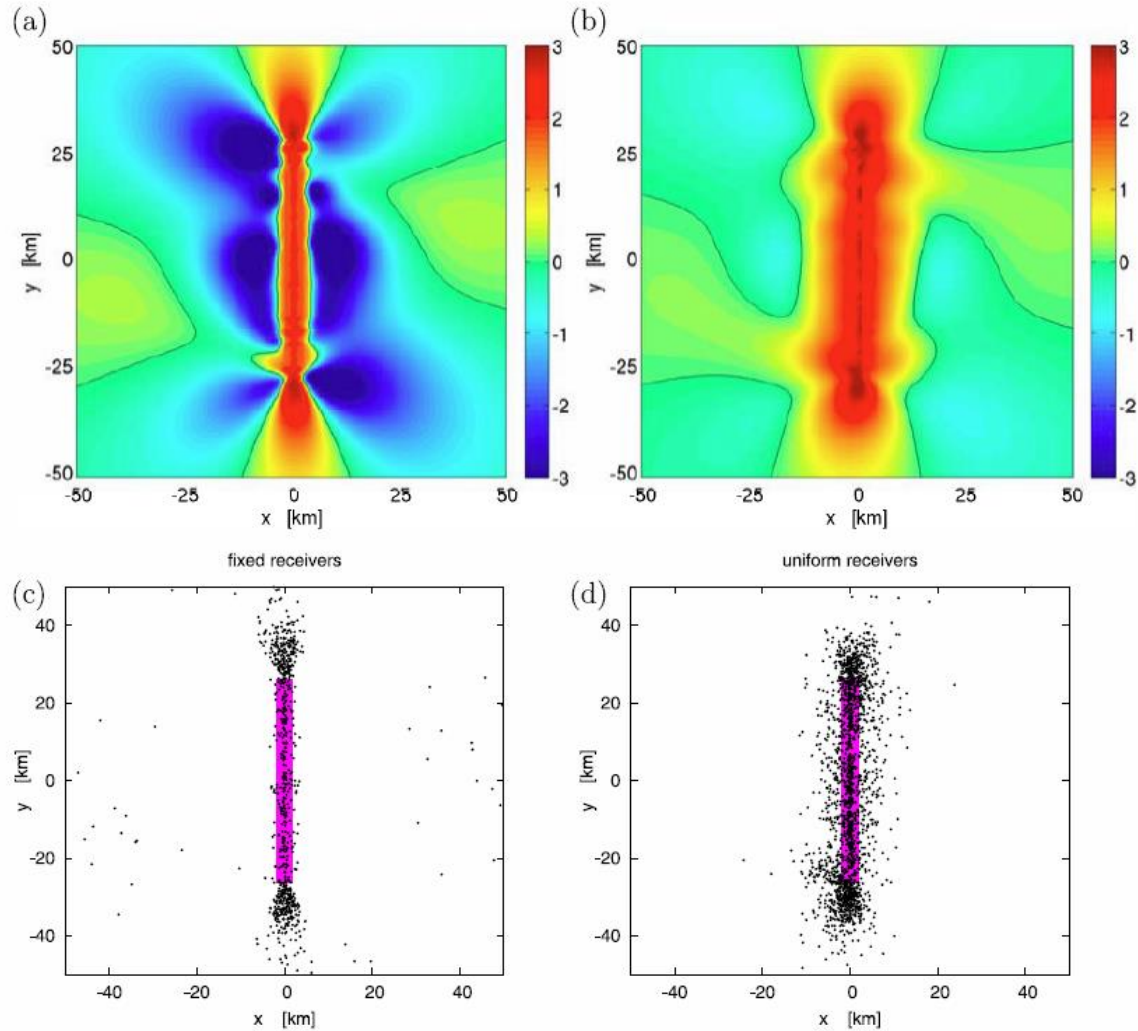


Figure 4

$$R(x, y) = \sum_k \int_{t_0}^T R(x, y, z_k, t) dt$$

Results, Spatiotemporal Pattern [32]

- *Spatial activation map: activation close to the main shock*

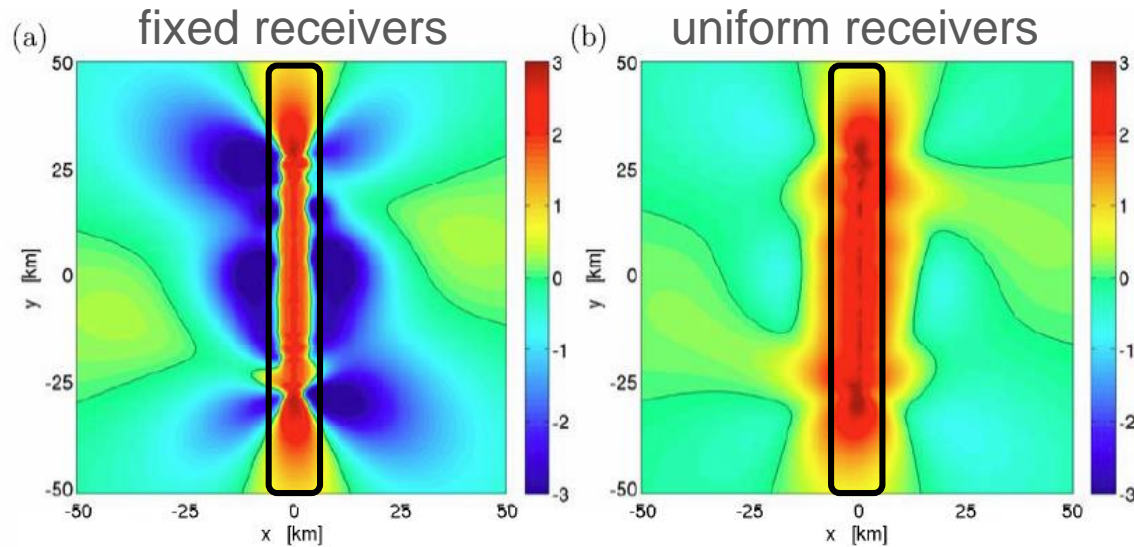


Figure 4a, b

- In both cases, it can be clearly seen that earthquake activation occurs *on and close to the main shock rupture*, due to the small-scale slip variability on the rupture plane.

The slip distribution with $H = 0.7$ leads locally to a stress increase there, although the mean stress within the rupture plane dropped significantly.

Results, Spatiotemporal Pattern [32]

■ *Spatial activation map: deactivation zone*

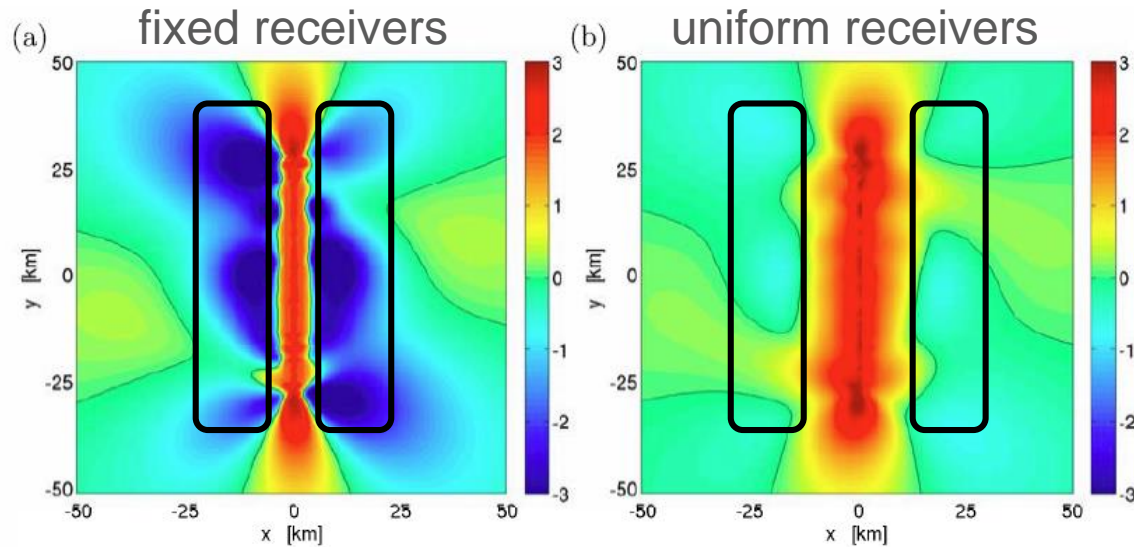


Figure 4a, b

- In the case of a unique receiver fault orientation (Fig. 4a), *a significant zone of deactivation exists a few kilometers away from the fault.*
- For more diverse receiver orientations (Fig. 4b), the activation belt around the fault becomes much larger and *the zones of deactivation are moved more than 20 km away.*

Results, Spatiotemporal Pattern [33]

■ *Spatial activation map: spatial aftershock distribution*

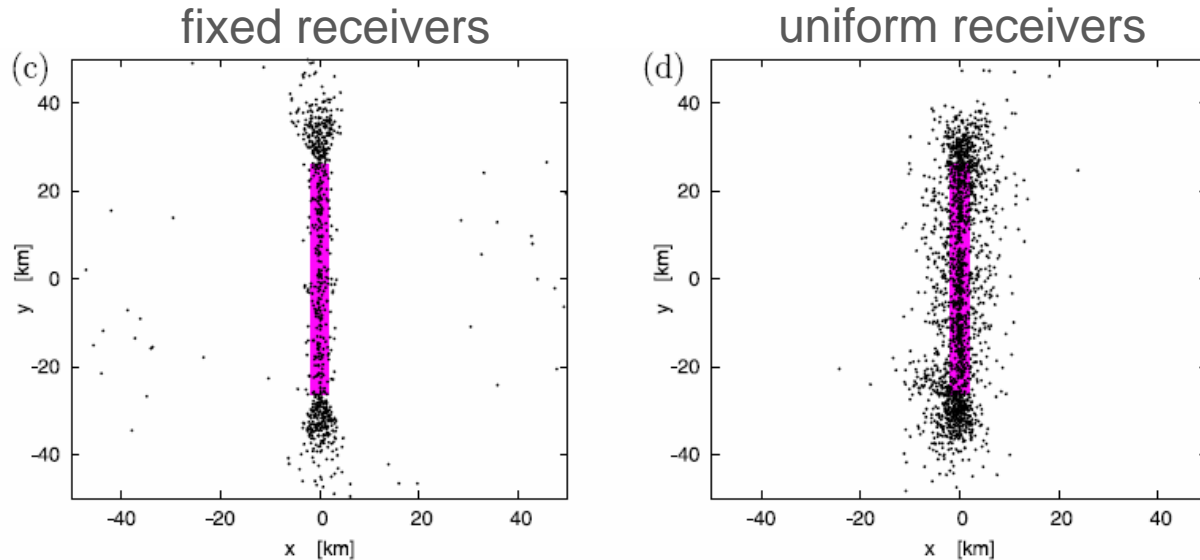


Figure 4c, d

- By using Monte Carlo simulation by the inverse transform method, corresponding spatial aftershock distributions are obtained.
- It becomes clear that the presence of *a large diversity* of fault orientations leads to significantly *higher on-fault activity* and an earthquake activation in *a broader zone* surrounding the main shock fracture.

Results, Diversity of Focal Mechanisms [34-36]

■ *Rotation of the stress*

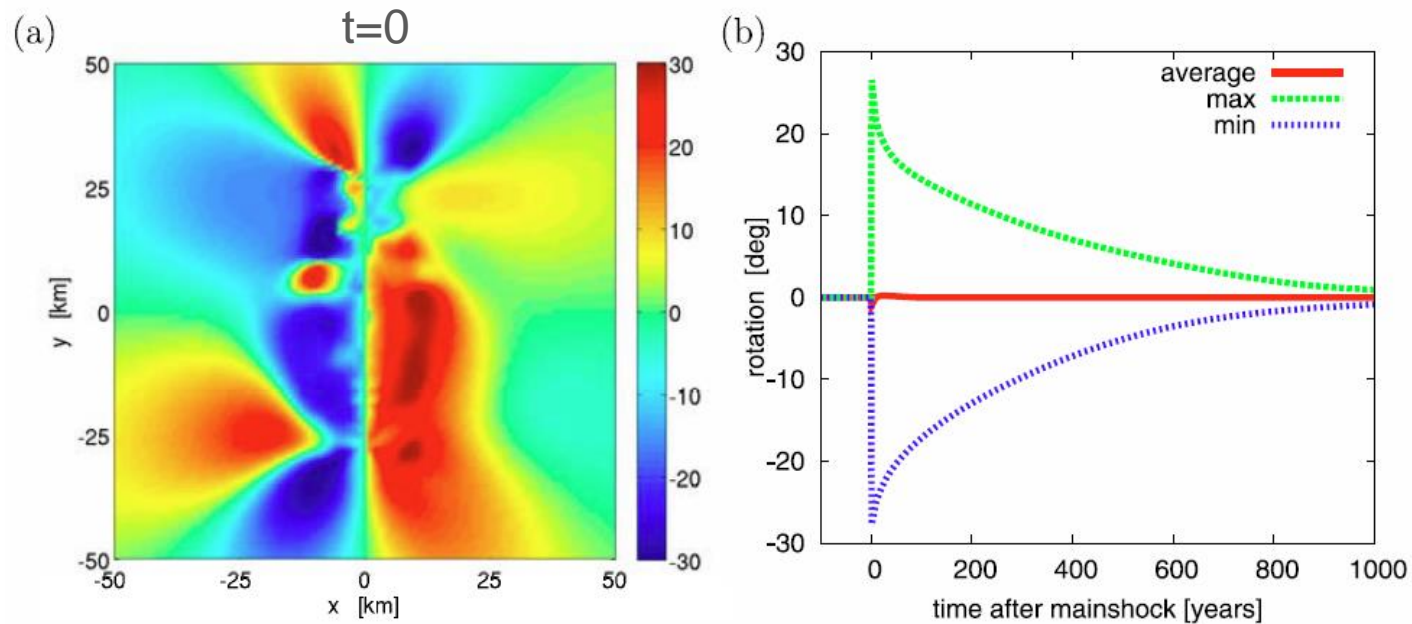


Figure 5

- This modeling also allows the analysis of the variability of the focal mechanism
- To analyze the potential rotation of the focal mechanism, *the average of the horizontal direction of the pressure axis is calculated.* (= the direction of the apparent maximum horizontal stress S_H)

Results, Diversity of Focal Mechanisms [35]

■ Spatiotemporal distribution of the rotation

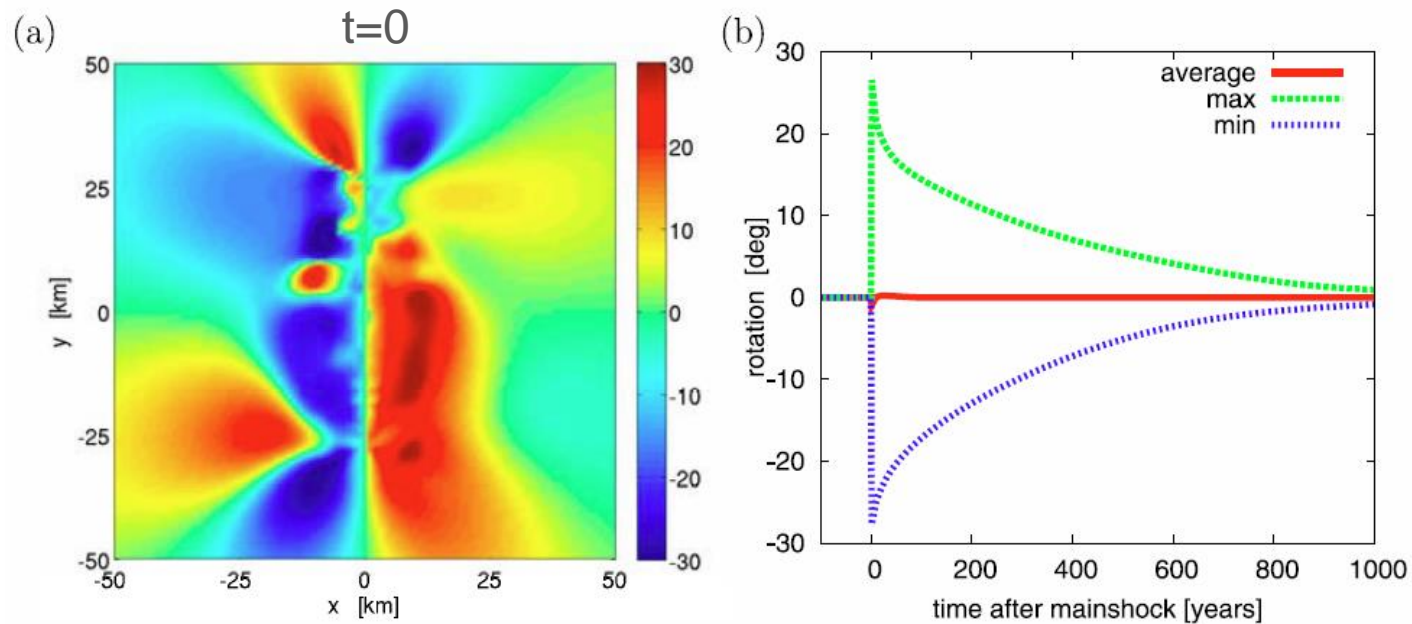


Figure 5

- The result shows that this rotation is very heterogeneous in space (Fig. 5a), but an average rotation of the whole region is insignificant.
- As for the temporal decay (Fig. 5b), while the average is always close to zero, the maximum and minimum rotations go back to its original value very slowly.

Results, Diversity of Focal Mechanisms [36]

■ *Comparison with the previous simulation*

- This result is comparable to the previous result of a rotation in the case of RSF nucleation *in heterogeneous stress fields* (Smith and Dieterich, 2010).
- The analysis of a distribution of receiver fault orientations with a homogeneous background rate and that of fixed optimally oriented fault planes with a heterogeneous stress fields lead the same result.
- However, the result of multiple fault orientations is independent of the absolute stress state.

Application to the Lander Sequence [37]

■ *Observation and model setting*

- 1992 M7.3 Landers earthquake occurred on 1992/06/28 with an epicenter -116.44° longitude and 34.20° latitude and triggered 1300 $M \geq 3$ aftershocks.
- For the model simulation, the slip model of the main shock is from Wald and Heaton (1994), the calculation of the stress changes used the code of Wang et al. (2006).
- The determination of the stresses and the aftershock rates are calculated in -117.5° — -115.5° W \times 33.5° — 35.3° N with 0.01° grid spacing, 3 km — 13 km in depth with 1 km grid spacing.
- An a value is 4.25, from declustering of the 1984-1991 earthquake activities.
- For a comparison, $M \geq 3$, directly triggered aftershocks of the catalog are used.

Application to the Lander Sequence [38]

■ Comparison of the observation and model forecasting

- The result show that fixed receiver faults is not able to reproduce the observation.

The forecasted total number of aftershocks is clearly smaller than the observation.

Many of the real aftershocks occurred in regions where the model predicts quiescence.

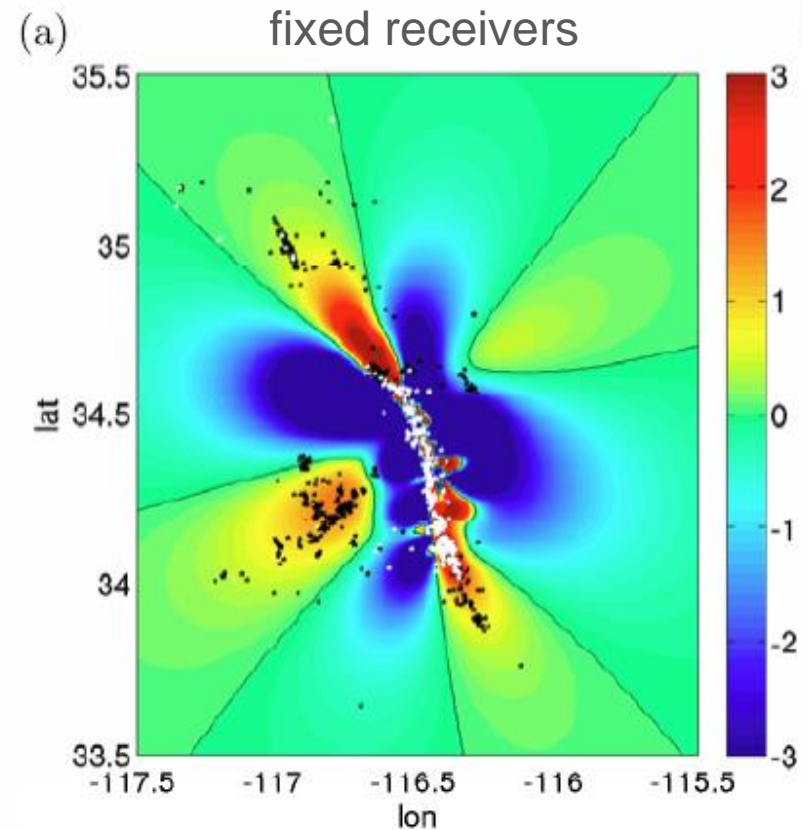
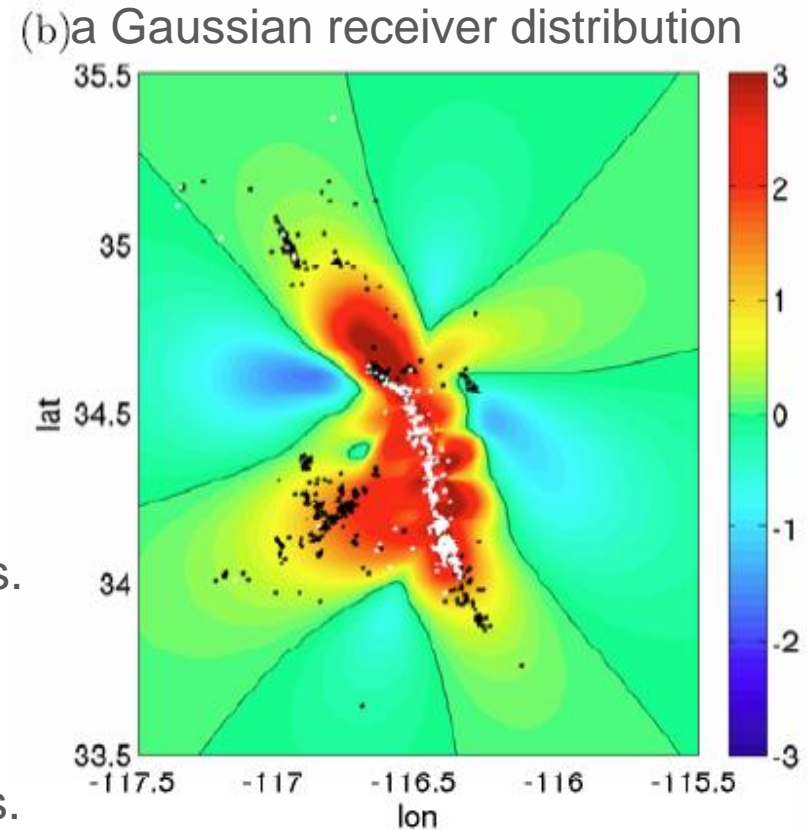


Figure 6a

Application to the Lander Sequence [38]

■ Comparison of the observation and model forecasting

- However,
if a Gaussian distribution of receiver orientation is assumed,
the spatiotemporal decay is in good agreement with the observations.
1.
The absolute number of $M \geq 3$ aftershocks is close to the observation, almost independent of other parameters.
 2.
The predicted spatial activation is in better accordance with the observations.



Application to the Lander Sequence [38]

■ Comparison of the observation and model forecasting

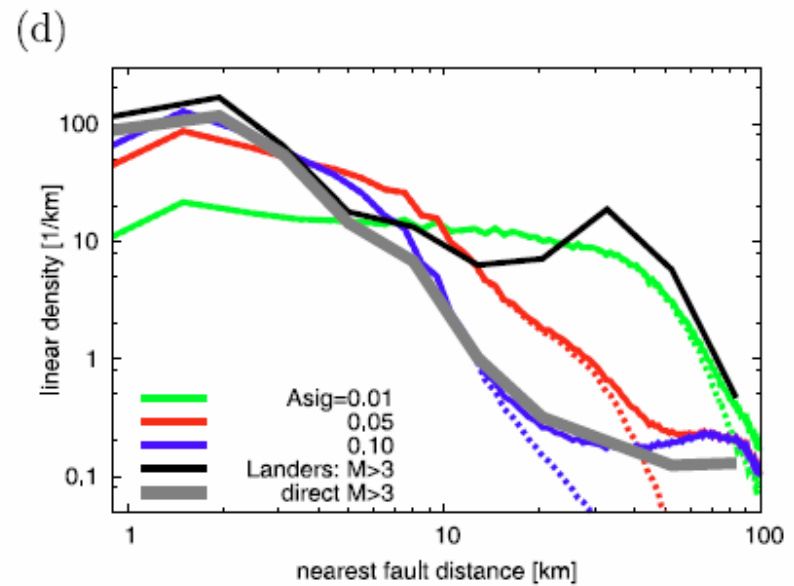
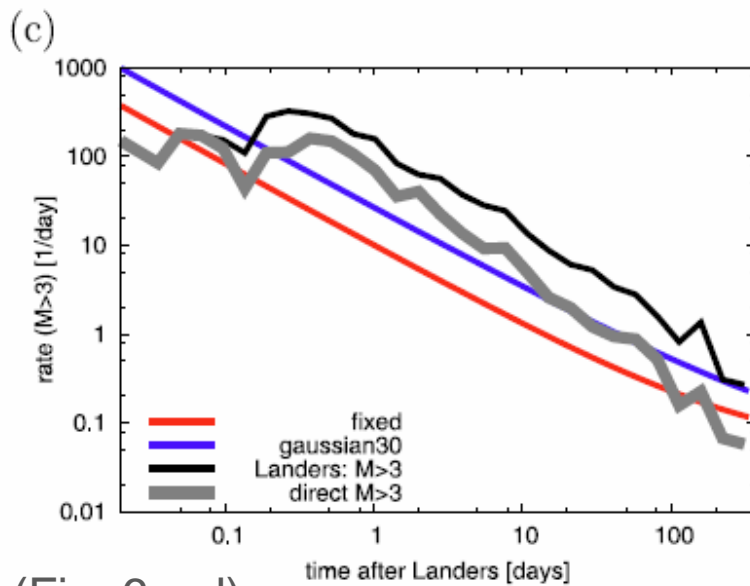


(Fig. 6c, d)

- The spatial decay (Fig. 6d) is close to one of the observed direct triggered events for $A\sigma = 0.1$ MPa, one of the total aftershock activity for $A\sigma = 0.01$ MPa.
- The $A\sigma$ value of 0.017 MPa inverted by Hainzl et al. (2009) for the same sequence with the stress-triggering model is rather an effective fitting parameter.

Discussion [39]

■ *Effect of the orientation of the pre-existing faults*

- In earthquake models based on stress interactions, *the preexisting fault structure* has to be specified.
- Usually, it is assumed *one particular orientation* for simplicity: fixed plane or optimal oriented fault planes.
- In this study, the effect of allowing ruptures to nucleate on *populations of preexisting faults* with different orientations
- The linear relation between background activity and tectonic loading is employed.

Discussion [40]

■ *Effect of the orientation of the pre-existing faults*

- This modeling shows that the *realistic distribution of receiver fault orientations* has a major impact on the predicted aftershock activity.
- This result is in general agreement with the previous study which considered another variability of the model parameters (stress field). (Hainzl et al., 2009)
- A number of other mechanisms and uncertainties will also add to such an effective distribution of stress values.
- However, the investigations of this study clearly show that *the fault structure* has a first order impact on earthquake forecasts.

Discussion [41]

■ *Model parameter dependence*

- One important result of this model is that the aftershock activity is almost *independent of the background rate*.

This result comes from the linear relation between background activity and tectonic loading.

- This insensitivity is good news for the predictive power of the model because the spatial-dependent background rate is not well-constrained.
- The forecast of the total aftershock productivity becomes almost *parameter-independent* by using this correlation.

Discussion [42]

■ *General problems of the model*

- The application to the Landers sequence also indicates two general problems of the model.

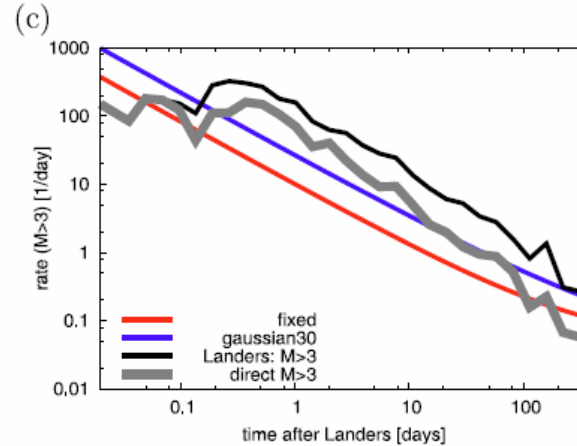


Figure 6c

- (1) The RSF model can only explain Omori exponents $p \leq 1$. The steeper decay of the Landers aftershock can only be explained postseismic processes.
- (2) Secondary aftershocks are ignored in the model. The implementation of them in the model is straightforward, but an adequate model would require high-resolution in space.

Discussion [43]

■ Spatial decay

- The spatial decay of the density of early aftershocks has been claimed to show a power law decay with $\eta \approx 1.4$.

However, Richards-Dinger and Stein (2009) demonstrated that the decay becomes much steeper if the background activity is appropriately taken in account.

- The result of this static stress triggering model showed a nonunique spatial decay which depends on the assumed receiver fault distribution as well as on the background level and the friction parameter.
- This spatial decay vary between an apparent power law decay and an exponential decay.

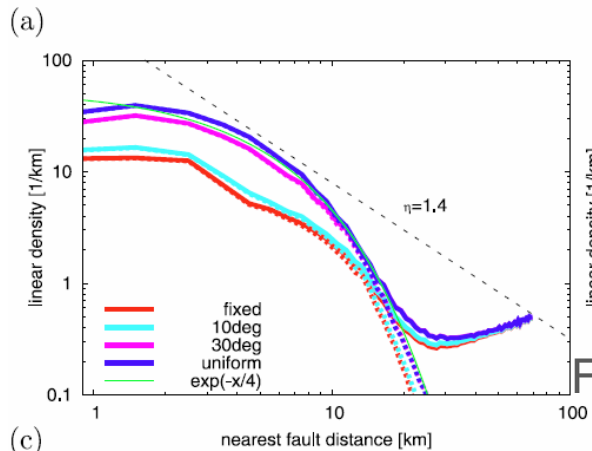


Figure 3a

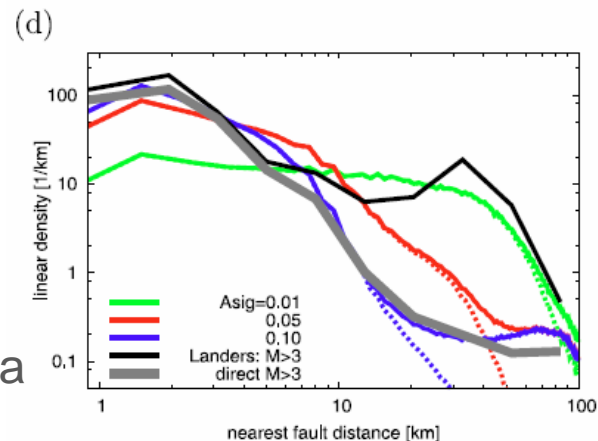


Figure 6d

Discussion [43]

■ Spatial decay

- This modeling indicates, for planar faults, the spatial decay is more similar to an exponential function. However, for nonplanar faults (Landers rupture), a more power-law-type is predicted.
 - ▶ Thus the geometry of the rupture surface may play an important role for the shape of the spatial decay.
- The Landers example also shows that this modeling cannot explain significant aftershock activation at >20 km
- This activation is mainly related to seven events in the NW, which is might related to the effect of dynamic-triggering.

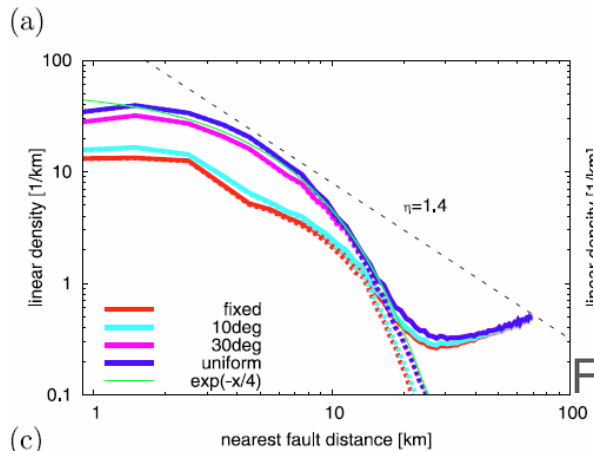


Figure 3a

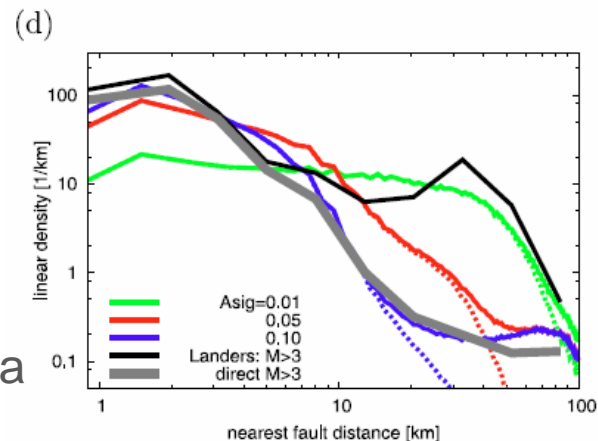


Figure 6d

Summary [44-46]

- In this study, earthquake simulations which are based on both physical (RSF, stress interaction, heterogeneous slip) and stochastic (populations of preexisting faults with different orientations) approach are used to bridge the gap between purely statistical and deterministic models.
- As a result of multiple fault plane orientations, quiet zones of aftershocks cannot be seen, which is in agreement with some observations. The spatial decay of the aftershock density depends on the model parameters as well as the fault geometry, and can be partly explained by a power law or an exponential function.
- The predicted level and time-dependence of the aftershock activity are insensitive to the model parameters due to the linear relationship between tectonic stressing and background rate. The application to the 1992 M7.3 Landers sequence shows that the model prediction is in agreement with the observations if broad distribution of preexisting fault orientation is assumed.